Journal of Applied Physics

# Design of resonant-cavity-enhanced multi-band photodetectors

Cite as: J. Appl. Phys. **110**, 043112 (2011); https://doi.org/10.1063/1.3626812
Submitted: 05 May 2011 • Accepted: 21 July 2011 • Published Online: 26 August 2011

**Yan-Feng Lao, Gamini Ariyawansa and A. G. Unil Perera**

J. Appl. Phys. **110**, 043112 (2011); https://doi.org/10.1063/1.3626812

**110**, 043112

JOURNAL OF APPLIED PHYSICS **110**, 043112 (2011)

# Design of resonant-cavity-enhanced multi-band photodetectors

Yan-Feng Lao, Gamini Ariyawansa, and A. G. Unil Perera[a]
*Department of Physics and Astronomy, Georgia State University, Atlanta, Georgia 30303, USA*

(Received 5 May 2011; accepted 21 July 2011; published online 26 August 2011; publisher error corrected 30 August 2011)

A theoretical analysis to improve the quantum efficiency of detectors sensing in multiple spectral bands is presented. The effective coupling between the incoming light and multiple absorbing regions for simultaneously improving the multi-band absorption efficiency is obtained by using resonant-cavity structures. An optimized cavity with only a Au bottom reflector gives rise to an enhancement factor of 11 in absorption compared to the conventional detector without the cavity. Further improvement, by a factor of 26, can be attained with the aid of a dual-band Bragg reflector placed at the top. The resulting multi-band resonant-cavity detector increases the response in three out of four detection bands contributing to the spectral range from visible to long-wave infrared (IR). The optimized detector is capable of serving multiple purposes, such as regular IR detection for atmospheric windows, gas sensing, and for optical communications. © *2011 American Institute of Physics*. [doi:10.1063/1.3626812]

## I. INTRODUCTION

Multiple infrared (IR) detection has been widely used for various applications such as land-mine detection, missile-warning sensors, identification of muzzle flashes from firearms, space situational awareness, and environmental monitoring. The reported multi-band detectors include HgCdTe[1] detectors, quantum well[2,3]/quantum dot[4,5] infrared photodetectors, and homo-/hetero-junction detectors.[6] A recent work reported by Ariyawansa *et al.*[2] demonstrated that a wide multi-spectral detection from visible (VIS) to long-wave infrared (LWIR) can be simultaneously covered in one detector architecture.

A multi-band detector typically consists of a multiple stack of absorbing elements, each of which responds to different wavelength regions. Normally, the short-wave detecting elements are placed on top of the long-wave ones to reduce the optical absorption loss of incoming radiation. However, there are two situations raising the issues of optical loss. First, the doped layers in the short-wave regions can cause free-carrier absorption loss, especially in the long-wavelength range. Second, in the case where the detector architecture requires a reverse order, the short-wave radiation could be greatly attenuated when first passing through the long-wave detecting region due to absorption such as inter-band transitions. Moreover, a large number of quantum wells (QWs) is usually needed to obtain considerable absorption which increases the thickness, especially in a detector with multi-groups of QWs sensing at different wavelengths. These issues can be avoided by using optical-coupling enhancement approaches, such as the use of a Fabry-Perot (F-P) resonant cavity. Resonant-cavity-enhanced (RCE) photodetectors have attracted much attention in the past to attain high quantum efficiency (QE), wavelength selectivity, and a high speed response.[7–9] The RCE detector usually responds in one spectral band by sandwiching the active region between reflectors such as metal and distributed Bragg reflectors (DBRs). The improvement is due to the optical-field enhancement as a result of standing waves being formed in the cavity. A specific design for obtaining high-field domains can be made for each of the absorbing elements for the highest optical coupling. This could compensate for the loss of incoming light and reduce the number of QWs without a loss in absorption.

Along with the field enhancement, a cavity structure creates a series of resonance modes at specific wavelengths, thus functioning as a built-in optical filter. This feature is desirable for multi-band detectors. To implement multi-band detection, various optical processes are employed, such as inter-band transitions in intrinsic materials and inter-subband transitions in QWs. The spectral response threshold is determined by either the fundamental bandgap or the separation of energy levels of QWs. A careful design should be carried out in order to minimize the spectral cross-talk, which is, to a certain degree, limited by the availability of materials or the quantum structure to be used. On the contrary, the spectral response of a detector can be conveniently tailored by employing a cavity in which the detection wavelengths at resonance gain the maximum electric field of light. Therefore, a multi-band resonant-cavity detector can make use of materials with a broad spectral response, such as the inter-valence-band transition-based response,[10] in contrast to quantum structures responding in a relatively narrow range. The advantage is that multi-band detectors can be fabricated based on a mature material system, such as GaAs/AlGaAs.

In this paper, the F-P resonant-cavity concept is implemented on multi-band detectors for simultaneous enhancement in multiple spectral ranges. The InP-based detector structures, schematically shown in Fig. 1, are expected to respond in visible-near-infrared (VIS-NIR), short-wave infrared (SWIR), mid-wave infrared (MWIR), and long-wave infrared (LWIR) regions.[2] By placing only a Au reflector at the bottom side (Fig. 1(b)) alone, three out of four active regions can be optimized to match the standing-wave

---

[a] Electronic mail: uperera@gsu.edu.

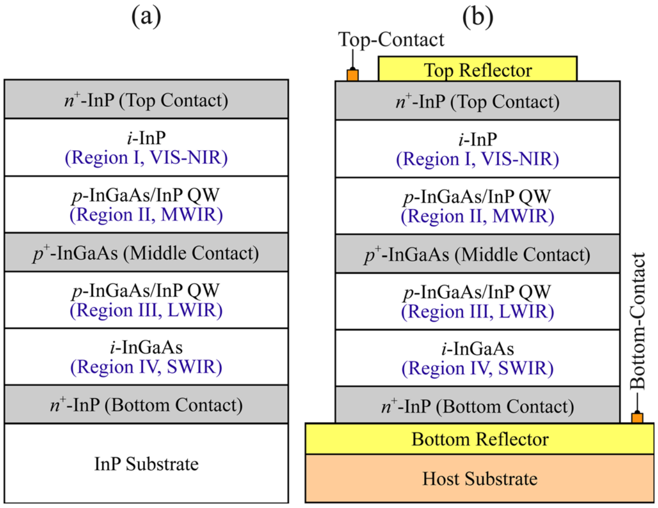

FIG. 1. (Color online) (a) A schematic of the conventional multi-band detector without the cavity. Regions I–IV correspond to four absorbing elements responding to different wavelengths. (b) The processed multi-band resonant-cavity detector with the active region sandwiched between two reflectors. A Au film is used as the bottom reflector, while the top reflector can be either a native semiconductor-air interface or a dual-band DBR.

patterns formed in the cavity, leading to an increase in the optical field. Further improvement is accomplished with the aid of another dual-band distributed Bragg reflector (DBR)[11] located at the top. In contrast to conventional DBR with only one high-reflection band, the dual-band DBR reported here acts as the reflectors for two spectral bands, SWIR and MWIR. The analysis shows an enhancement in the short-wave ranges, while the LWIR remains the same as the one with only the Au bottom reflector. A specific application was made to a GaAs multi-band detector, reported in Ariyawansa *et al.*'s work,[2] showing improvements in the responsivity or tailoring the spectral response toward the desired wavelengths.

## II. THEORETICAL MODELS

Ünlü *et al.*[7] have discussed the formulation of RCE effects with analytical expressions by appropriate approximations, such as neglecting the interface reflection between similar materials. In the current work, calculations on the optical properties of detectors will be carried out on the basis of the transfer-matrix method (TMM)[12] without approximations. The accuracy of the calculations depends on the input parameters, i.e., the complex index of refraction of each stratified layer. In order to compute the range from VIS to LWIR, various optical processes[13] such as inter-band transitions, phonon, and free-carrier absorption are included in the modeling of the refractive index. The imaginary component of the dielectric function (DF) is first calculated and then the Kramers-Kronig (KK) transformation is applied to obtain the complex DF which yields the complex index of refraction. The procedure computing the DF is detailed in the Appendix. More details can be found in Ref. 13.

The stack of epitaxial layers are assumed to be along the $z$-axis (epitaxy direction) with the origin at the topmost surface and the positive direction pointing toward the substrate. As a result of the interfacial reflection, there exist forward and backward traveling waves in one layer, labeled as $j$. In the following, $j = 1$ denotes the topmost layer and $N$ is the total number of layers. For a transverse electric (TE) polarization of incident light, the electric field is given by

$$\boldsymbol{E}^j = \left[A_j e^{ik_z^j(z-z_j)} + B_j e^{-ik_z^j(z-z_j)}\right] e^{ik_x^j x} \cdot \hat{\boldsymbol{e}}_y, \tag{1}$$

in which $\hat{\boldsymbol{e}}_y$ is a unit vector of the $y$-axis perpendicular to the incident plane, $k_x^j$ ($k_z^j$) is the $x(z)$ component of the wave vector $\boldsymbol{k}^j$ in the layer $j$, $z_j$ is the coordinate of the interface between layer $j$ and $j+1$, named interface $j$, and $A_j$ and $B_j$ are the amplitudes of the forward and backward waves, respectively. The magnetic field, $\boldsymbol{H}^j$ is calculated from the Maxwell's equations by $\boldsymbol{H}^j = \nabla \times \boldsymbol{E}^j / i\omega\mu_j$, in which $\omega$ is the angular frequency and $\mu_j$ is the permeability of free space. By applying the boundary conditions, i.e.,

$$E_y^{j-1}(z_{j-1}) = E_y^j(z_{j-1}) \text{ and } H_x^{j-1}(z_{j-1}) = H_x^j(z_{j-1}), \tag{2}$$

the transfer matrix can be deduced as

$$M_{j-1,j} = \frac{1}{2}\begin{bmatrix} \left(1+\frac{P_j}{P_{j-1}}\right)e^{-i\beta_j} & \left(1-\frac{P_j}{P_{j-1}}\right)e^{i\beta_j} \\ \left(1-\frac{P_j}{P_{j-1}}\right)e^{-i\beta_j} & \left(1+\frac{P_j}{P_{j-1}}\right)e^{i\beta_j} \end{bmatrix}. \tag{3}$$

Here, $M_{j-1,j}$ connects the electric field of light in the layers beside the interface $j$ through

$$\begin{bmatrix} A_{j-1} \\ B_{j-1} \end{bmatrix} = M_{j-1,j}\begin{bmatrix} A_j \\ B_j \end{bmatrix}. \tag{4}$$

In Eq. (3), $P_j = k_z^j/\omega\mu_j$ and $\beta_j = k_z^j d_j$ with $d_j = z_j - z_{j-1}$, where $d_j$ is the thickness of layer $j$. For $j = N+1$, which represents the light outgoing media, the transfer matrix is calculated by setting $d_{N+1} = 0$. The formalism of the transfer matrix for the transverse magnetic (TM) polarization of incident light can be conveniently deduced using the duality principle, i.e., $\boldsymbol{E} \to \boldsymbol{H}$, $\boldsymbol{H} \to -\boldsymbol{E}$, $\mu \to \varepsilon$, and $\varepsilon \to \mu$ which leads to the same expression of Eq. (3), with $P_j$ replaced by $k_z^j/\omega\varepsilon_j$.

The electric and magnetic fields in each layer can be solved by repeating Eq. (3). The total transfer matrix, $M$ is the multiplication of the matrix in layer 0 through layer $N+1$ ($j = 0$ representing the light incoming media), i.e., $M = {}_{j=1}^{N+1} M_{j-1,j}$, which gives the reflectivity, $R$, and transmissivity, $T$, expressed by

$$R = \left|\frac{M_{21}}{M_{11}}\right|^2 \text{ and } T = \frac{\mathrm{Re}(P_{N+1})}{\mathrm{Re}(P_0)} \cdot \left|\frac{1}{M_{11}}\right|^2. \tag{5}$$

Following Ünlü's discussion[7] on the QE, the optical power is proportional to the squared electric field, i.e., $\sim n_r|E_y|^2$, where $n_r$ is the real part of the complex refractive index. Defining the absorption efficiency $\eta_\alpha$ as the ratio of the absorbed optical power to the incident power, $\eta_\alpha$ should read

$$\eta_\alpha = \Gamma_{en} \cdot \alpha_j d, \tag{6}$$

with

$$\Gamma_{en} = \frac{1}{n_{r0}\left|E_{y0}\right|^2} \cdot \frac{1}{d} \sum_j \int_j n_{rj} \left|E_y^j(z)\right|^2 dz. \tag{7}$$

Layer $j$, having the homogeneous absorption coefficient $\alpha_j$, constitutes the absorbing elements of the active region in the detector. The total thickness is calculated by $d = \sum_j d_j$. Here, $\Gamma_{en}$ is the ratio of the averaged optical power in the active region to the incident power. Clearly, $\Gamma_{en}$ is determined by the magnitude of the optical field and the overlap between the active region and the field which are the subject of F-P cavity optimization.

The maximization of the optical field usually resorts to the resonance condition at which the round-trip phase is an integer multiple of $2\pi$, i.e.,

$$2k_m L_c + \varphi_1 + \varphi_2 = m \cdot 2\pi, \tag{8}$$

where $k_m$ is the wave vector of the $m$th resonance mode, defined as $k_m = 2\pi n_{eff}/\lambda_{cm}$, with $n_{eff}$ being the effective refractive index of the cavity, and $\lambda_{cm}$ the corresponding wavelength, $\varphi_1$ and $\varphi_2$ are the phase shifts at the top and bottom reflectors, respectively, and $L_c$ is the physical cavity length. In the present study, reflectors such as the Au film, DBR, and the native semiconductor-air interface will be used. The phase shift can easily be calculated using the TMM which gives either the $\pi$ or 0 phase change. Hence, the optical length of the cavity ($n_{eff}L_c$) primarily determines the resonance modes.

Another crucial quantity is the wavelength spacing between neighboring modes which can be derived from Eq. (8) as[7]

$$\Delta\lambda_c = \frac{\lambda^2}{2n_{eff}(L_c + L_{eff,1} + L_{eff,2})}, \tag{9}$$

where $L_{eff,i}$ is the effective length of the top ($i = 1$) and bottom ($i = 2$) reflectors.[7] It is evident that the spacing of modes at the long-wavelength range is larger than that at the short-wavelength range. For example, in the case of using the Au reflector alone, the mode spacings around 10 and 4 $\mu$m are nearly 4 and 1 $\mu$m, respectively. Therefore, the optimization in the long-wave region is much more critical than that in the short-wave region. Additionally, a specific consideration will be made to the short-wave region by using a dual-band DBR, as dictated in the following section.

## III. RESULTS AND DISCUSSION

The QE is proportional to the absorption efficiency ($\eta_\alpha$) and the carrier escape probability.[9,14] Since the current investigation concentrates on the optimization of optical performance without addressing the electrical properties, the carrier escape probability remains unchanged. An increase in the $\eta_\alpha$ thus yields the same increase in the QE and hence, the spectral responsivity.

Figure 1 shows the InP-based multi-band detector structure consisting of two back-to-back connected *p*-*i*-*n* photodiodes.[2] Regions I, II, III, and IV respond in VIS-NIR, MWIR, LWIR, and SWIR, respectively, by virtue of the optical processes due to inter-band transitions in the *i*-InP, inter-subband transitions in *p*-InGaAs/InP QWs, and the inter-band transitions in *i*-InGaAs. The *i*-InGaAs region IV will be lattice-matched to InP, giving the threshold wavelength at 1.7 $\mu$m, while either lattice-matched or strained InGaAs layers can be used in the QW regions II and III to implement MWIR (3–5 $\mu$m) and LWIR (8–14 $\mu$m) detection, e.g., in Refs. 15 and 16. The detector structure under optimization has a similar structure to the experimentally demonstrated multi-band detector using the GaAs-based material system.[2] When a negative (positive) bias is applied to the top contact, the bottom (top) *p*-*i*-*n* diode under reverse bias is sensing the incoming light, while the band profile of the top (bottom) diode under forward bias is close to the flatband condition, making it inactive for photo-carrier generation. Therefore, the detector shows wavelength selectivity depending on the bias polarity applied.

Due to the detector configuration, one intrinsic region, i.e., *i*-InGaAs, lies at the bottom side of the detector. An unnecessary loss of incoming light occurs at layers other than region IV, especially due to the $p^+$- InGaAs middle-contact region which is required to fabricate a metallic ohmic contact. Moreover, the loss of the LWIR radiation is due to the free-carrier absorption in the doped top and middle contact layers. The use of a cavity structure for effective optical coupling is thus desirable. Since the InP constitutes the main material of the detector, significant absorption in the VIS-NIR greatly reduces the F-P cavity effects. Region I is thus placed right under the top contact layer. In the following, the optimization on three out of four detection bands is carried out.

To fabricate a F-P cavity, appropriate reflectors should be applied. A Bragg reflector normally consists of two alternating quarter-wave ($\lambda_0/4$) layers of high-index and low-index materials. To attain the high reflection in the LWIR, the DBR thickness will exceed the limitation of material growth capability and hence, may be not practical. On the contrary, a Au film is capable of acting as a good reflector over the whole spectral range, e.g., a reflectivity of 98% for the InP-Au configuration, and is thus adopted as the bottom reflector. The resonant-cavity detector can be fabricated by using techniques such as metallic wafer bonding,[17] by which a Au reflector is deposited at the bottom of the active region and the whole structure will sit on a host substrate, such as the Si substrate. Using wet chemical etching, the original InP substrate can be removed and then the sample is processed into mesas, resulting in the final detector structure shown in Fig. 1(b). The top reflector can be the native InP-air interface which has the reflectivity varied from 27% at 1.5 $\mu$m to 17% at 12 $\mu$m.

The locations of the resonance modes are primarily determined by the cavity to which the optimizing was made. In Fig. 2 the reflection spectrum is shown, dictating the resonance dips (dashed line). As mentioned (Eq. 9), the mode spacing is proportional to the wavelength. In the LWIR region, only one mode lies in the detection range of interest. Thus, the cavity should be properly adjusted. The optimization should also be able to maximize the overlapping between the optical field and the absorbing elements. With such considerations in mind, Fig. 3 plots the absorption

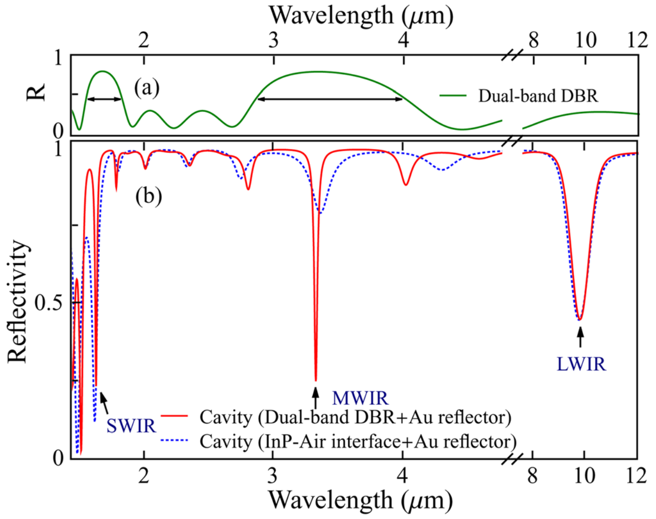

FIG. 2. (Color online) Calculated reflection spectra of (a) a 3-period $TiO_2$/$SiO_2$ dual-band DBR, and (b) whole resonant-cavity detector structures. The use of only a Au reflector (dotted line) produces resonance modes (the dips) in the whole spectral region. The solid line shows further resonance enhancement by using a SWIR-MWIR dual-band DBR without affecting the LWIR performance. Both resonance modes lie within DBR's high-reflection bands. Resonance modes for the regions of interest IV (SWIR), II (MWIR), and III (LWIR) are indicated by arrows.

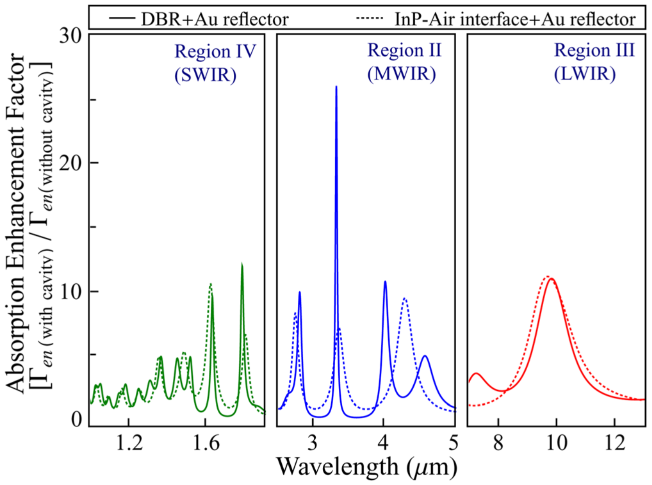

FIG. 3. (Color online) Calculated absorption enhancement factor for the absorbing regions II, III, and IV, which is defined as the ratio of $\Gamma_{en}$ for a detector with the cavity to that without the cavity. A factor of 11 is achieved by placing a Au reflector at the bottom side of the detectors, while the use of another top 3-period $TiO_2$/$SiO_2$ dual-band DBR gives rise to enhancement by a factor of 26.

enhancement factor for three detection bands. The enhancement factor is defined as the ratio of $\Gamma_{en}$ for the detector with the F-P cavity to that without the cavity. The maximum enhancement for region IV (SWIR), II (MWIR), and III (LWIR) is reached at the factors of 10.5, 9.5, and 11, respectively. A clear view of the optical field, shown in Fig. 4, for the wavelength at resonance accounts for the enhancement. In each of the absorbing regions, the optical field is enhanced in comparison with the conventional structure without the cavity, except for region I (VIS-NIR). For region I, the incoming light at 0.8 μm is completely absorbed in its first travel by the inter-band transition in InP. In contrast, InGaAs is only used for the middle contact and for region IV (SWIR). Although inter-band transition occurs in the InGaAs, F-P enhancement can be still attained. In the case of ideal detectors,[2] where only two contacts (the top and bottom contacts) are needed, the $p^+$-InGaAs middle contact layer being replaced by $p^+$-InP should result in further improvement.

The use of a F-P cavity with the Au bottom reflector gives rise to simultaneous improvement in the absorption and the QE in three out of four detection bands, as seen in Fig. 3. As noted, the top reflector is yet to be optimized. Metallic reflectors such as a Au film with a thickness of 4 nm and gratings[18,19] are appropriate for the LWIR enhancement. Although the DBR is not practical for the LWIR, it acts as a good reflector for the SWIR and MWIR, and can also be grown in experiments, such as the semiconductor DBR using the epitaxial method and the oxide DBR using the conventional deposition method.[20] Here, a specifically designed DBR simultaneously performing as the reflector for the SWIR and MWIR is used.

The conventional DBR has a high-reflection band around $\lambda_0$, at which the reflection at each interface is in phase. For the same reason, other high-reflection bands come at wavelengths of $\lambda_0/2$, $\lambda_0/4$,…. All of the short-wavelength reflection bands are fixed once $\lambda_0$ is chosen. To be able to flexibly control high-reflection bands to desirable wavelengths, an alternative design is to use the dual-band DBR[11] in which one period consists of more than two layers. In order to simultaneously obtain high reflection at two wavelengths, $\lambda_1$ and $\lambda_2$, a phase factor $[\cos(2k_1 d) + \cos(2k_2 d)]$ ($k = 2n\pi/\lambda$, where $n$ is the refractive index) needs to be maximized. The dual-band DBR still consists of two materials but different layer configurations. The layer thickness $d$ is chosen to equal $\lambda_0/4n$ with $\lambda_0$ given by $\lambda_0 = 2\lambda_1\lambda_2/(\lambda_1 + \lambda_2)$. These two materials are then used to construct one repeating unit with the layer numbers calculated as $\Delta\lambda/\lambda_0$, where $\Delta\lambda = 2\lambda_1\lambda_2/(\lambda_2 - \lambda_1)$. Basically, the $\lambda_1$ and $\lambda_2$ can be arbitrarily designed depending on the structural parameters used. In Fig. 2(a) a dual-band DBR is shown, with one period consisting of 378.5-nm $SiO_2$, 264.8-nm $TiO_2$, and 264.8-nm $TiO_2$, resulting in two reflection bands centered at $\lambda_1 = 1.6$ μm and $\lambda_2 = 3.3$ μm. The refractive indexes of $SiO_2$ and $TiO_2$ were fitted to experimental data taken from Refs. 21 and 22 by the Sellmeier equation, $n(\lambda)^2 = a + b/[1 - (c/\lambda)^2]$, where $a$, $b$, and $c$ are the fitting parameters.

The dielectric $TiO_2$/$SiO_2$ DBR is transparent to the VIS-NIR region and has a trivial effect on region I. This material can be grown on the semiconductor surface, as previously used as one of the reflectors for the vertical-cavity lasers.[20] Figure 2 shows the calculated reflection spectrum of the detector structure with a dual-band DBR at the top and a Au reflector at the bottom. In comparison with the one without the top DBR, dips at 1.635 and 3.325 μm are the two resonance modes being enhanced by both the DBR and Au reflectors. As shown in Fig. 3, enhancement factors of 12 and 26 for region IV (SWIR) and region II (MWIR) are observed. In comparison with the case using the Au reflector

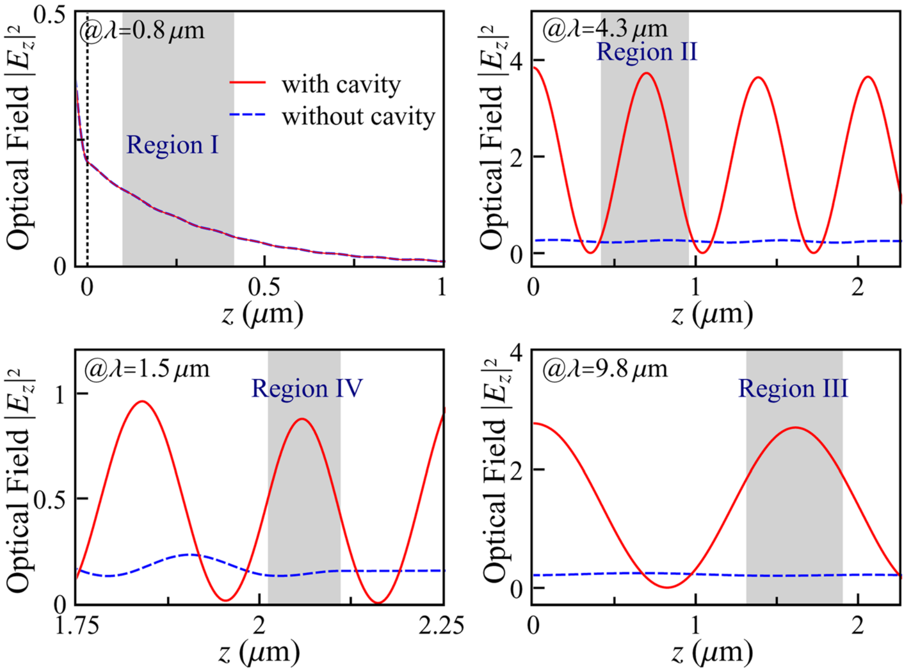

FIG. 4. (Color online) Comparison of optical field $|E_z|^2$ for light at 0.8, 1.5, 4.4, and 9.8 μm between the multi-band detectors with a resonant cavity and without the cavity, where the cavity structure consists of a Au reflector alone. The $z$-axis denotes the direction along with the growth direction. In each of the figures, the shadow area shows the enhanced field in the region of interest, except for region I in which the field remains unchanged due to InP absorption.

alone, the improvement in SWIR is not significant due to the InGaAs absorption. Reducing its thickness, such as replacing the middle contact layer with InP, will further increase the F-P effects. Furthermore, the use of dual-band DBR narrows the response peaks of both the SWIR and MWIR, which can be useful for monitoring gases by simultaneously identifying two absorbing lines. By selecting three periods of the DBR, the resonance at LWIR remains valid yielding a nearly fixed enhancement factor. This is because that the DBR is no longer a good reflector for the LWIR range, as seen in Fig. 2(a), and hence its effect only changes the cavity length for the LWIR region.

As an application, the F-P cavity optimization was applied to the already demonstrated GaAs multi-band detector with the structure shown in Ref. 2. Since the AlGaAs constitutes both the $i$-region and the barriers in the GaAs QWs, considerable absorption for light below 1.0 μm occurs, significantly degrading the F-P effects. Therefore, cavity optimization is only made to the QW regions responding in the 3–8 and 9–13 μm ranges. The final structure is similar to the one shown in Fig. 1. Since the detector consists of two groups of $n$-type QWs, the incoming light is assumed to be TM polarized with a 45° incidence angle. Since optimization only addresses the optical properties without any modifications on the electrical performances, the expected improvement in thespectral response should be proportional to the enhancement of absorption. The comparison of the spectral response in the cavity-enhanced multi-band detectors with the experiment is shown in Fig. 5. In this case, a single high-reflection type of conventional DBR (3 periods) is used for the MWIR alone since no SWIR optimization is required. The maximum enhancement factors for MWIR and LWIR are 5.5 and 9.5, and 17 and 9 corresponding to the structure with the Au reflector alone, and both the DBR and Au reflectors, respectively. It can be seen that the use of the F-P cavity also reduces the unnecessary response outside the spectral range of interest. For example, the ratio of the peak responsivity in the 3–4 μm range to that in the 4–8 μm range is increased from 3 in the original structure without the cavity up to 9 in the cavity-enhanced detector. The expected response by cavity enhancement is promising for designing optimized multi-band detectors with higher performances as well as the desired spectral response.

The results shown in Figs. 3 and 5 present an interesting feature. Narrow spectral responses are obtained in the SWIR and MWIR regions, while the LWIR response remains unchanged. This feature can be used for potential multi-

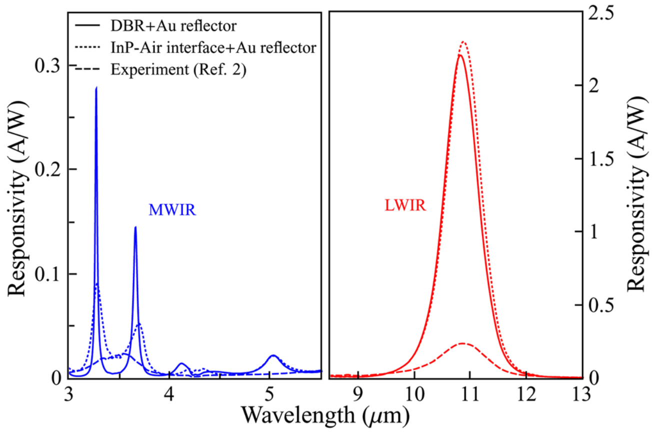

FIG. 5. (Color online) The optimization of the spectral response in a GaAs multi-band detector (see Ref. 2) by applying the F-P resonant cavity. The dotted and solid curves correspond to two cavity structures using a Au reflector, and both DBR and Au reflectors, respectively. The F-P resonance effects enhance the optical field and hence the QE, and also cause the splitting of the response peak between 3–4 μm. The DBR is designed such that enhancement only occurs in MWIR without affecting the LWIR.

purpose detectors. For example, the optimized multi-band resonant-cavity detector covers the atmospheric windows (3–5 and 8–14 $\mu$m), while the narrow response peaks will be useful for the monitoring of gases such as $H_2O$, $CO_2$, $N_2O$, and $NH_3$. By simultaneously measuring two absorption lines from the same gas, false positives will be greatly reduced. Additionally, the SWIR will also cover the important fiber optical communication band between 1.3–1.6 $\mu$m.

## IV. SUMMARY

To conclude, a detailed analysis to improve the QE of multi-band detectors has been carried out. In a multi-band detector, the performance could suffer from a low efficiency of absorption due to the multiple stack of absorbing elements, each of which responds to different wavelengths. The F-P cavity structure has been shown to be an effective approach for the simultaneous enhancement of optical coupling on three out of four detection bands. Two approaches were reported. One is to use a Au reflector at the bottom side of the detectors and a native semiconductor-air surface as the top reflector. Enhancement in SWIR, MWIR, and LWIR was attained. Further optimization can be carried out by using a SWIR-MWIR dual-band DBR, causing significant enhancement in the corresponding spectral ranges. The optimized detector is capable of serving multiple purposes, such as regular IR detection for the 3–5 and 8–14 $\mu$m atmospheric windows, gas monitoring, and the optical communication field.

## ACKNOWLEDGMENTS

This work was supported in part by the US Army Research Office under Grant No. W911NF-08-1-0448, monitored by Dr. William W. Clark, and, in part, by the US National Science Foundation under Grant No. ECS-0553051.

## APPENDIX: DIELECTRIC FUNCTION MODEL

The complex dielectric function (DF) ($\varepsilon = \varepsilon_1 + i\varepsilon_2$) is determined by various optical processes, including the interband transitions and photon-phonon interactions (lattice absorption). If semiconductors are doped, intra-band (known as free-carrier absorption for both *n*- and *p*-type dopings) and inter-valence band (IVB) transitions (for *p*-type doping) should be taken into account. The modeling details have been described in Ref. 13. Here, a brief description is presented.

For a *p*-type semiconductor, three IVB transitions can occur among the valence bands (VBs), i.e., the split-off (*so*), light-hole (*lh*), and heavy-hole (*hh*) bands. Under an approximation of using parabolic-band structures, which is valid for most of the doping concentrations since transitions primarily occur around the $\Gamma$ point, the IVB contribution to the dielectric function can be expressed by

$$\varepsilon_2^{\mathrm{IVB}}(E) = \varepsilon_2^{12}(E) + \varepsilon_2^{13}(E) + \varepsilon_2^{23}(E), \qquad \text{(A1)}$$

in which the terms, in order, correspond to the *lh*-*hh*, *so*-*hh*, and *so*-*lh* transitions, respectively. For one transition taking place between bands $a$ and $b$ ($a, b = 1, 2, 3$), the DF is given by

$$\begin{aligned}\varepsilon_2^{ab}(E) = A_{ab}\frac{|E-(E_{b0}-E_{a0})|^{3/2}}{E^2}\frac{p}{(k_BT)^{3/2}}\\ \times\left[\exp\left(\frac{E_a}{k_BT}\right)-\exp\left(\frac{E_b}{k_BT}\right)\right]\cdot C_{FD}^{ab}.\end{aligned} \qquad \text{(A2)}$$

Here, $p$ is the hole concentration, $k_B$ is the Boltzmann constant, $T$ is the temperature, and $E_{a(b)}$ is given by the parabolic-band form, $E_{a(b)} = -E_{a(b)0} - \hbar^2k^2/2m^*_{a(b)}$ with $E_{a(b)0}$ and $m^*_{a(b)}$ being the band-edge energy and effective mass for band $a(b)$. In Eq. (A2), $E_a$ and $E_b$ are determined by $E_a - E_b = E$ and $C_{FD}^{ab}$ is a constant related to the Fermi level. For the non-degenerate semiconductor (low doping), $C_{FD}^{ab} \approx 1$ can be used. Here, $A_{ab}$ accounts for the transition strength and other effects such as the non-parabolicity of energy bands off the $\Gamma$ point. The fitting[13] to *p*-GaAs and *p*-$\mathrm{Ge}_{1-y}\mathrm{Sn}_y$ indicates that $A_{ab}$ is constant except at the higher doping range above $10^{19}\mathrm{cm}^{-3}$ as a result of the band non-parabolicity.

The computation of inter-band transitions caused by the DF involves several critical points (CPs) in the $\boldsymbol{k}$ space. These CPs are associated with singularities of the joint-density-of-states, satisfying $\nabla_k\left[E_i(\boldsymbol{k}) - E_j(\boldsymbol{k})\right] = 0$ ($i$ and $j$ are the band indexes). Additionally, the computation needs to include the continuum exciton contributions, i.e., band-to-band Coulomb enhancement effects. The formalism of the final DF was presented in Ref. 13 and is thus not repeated here. To be able to compare with experiments, the line-shape broadening is introduced by convoluting the unbroadening DF with a line-shape function.

Contributions of the free-carrier intra-band transition based on the classic Drude theory and phonon absorption modeled as harmonic oscillators have been explored in previous works.[8,9] The complex DF, which is mostly in the far-infared (FIR) range, can be given by

$$\varepsilon^{\mathrm{FIR}}(\omega) = \varepsilon_\infty\left[1 - \frac{\omega_p^2}{\omega(\omega + i\gamma)}\right] + \frac{S\cdot\omega_{\mathrm{TO}}^2}{\omega_{\mathrm{TO}}^2 - \omega^2 - i\omega\Gamma}, \qquad \text{(A3)}$$

where $\omega$ is the light frequency in wave numbers, $\varepsilon_\infty$ is the high-frequency dielectric constant, $\omega_p$ and $\gamma$ are the plasmon frequency and damping constant, $\omega_{\mathrm{TO}}$ and $\Gamma$ are the transverse optical (TO) phonon frequency and damping constant, and $S$ is the oscillator strength.

The total complex DF was computed by adding up all the DF imaginary components, i.e., $\varepsilon_2 = \varepsilon_2^{\mathrm{IVB}(\Gamma)} + \varepsilon_2^{\mathrm{BBCE}(\Gamma)} + \varepsilon_2^{\mathrm{FIR}}$, where the superscript ($\Gamma$) represents the broadening DF and $\varepsilon_2^{\mathrm{FIR}}$ is the imaginary component of Eq. (A3), and then applying the Kramers-Kronig (KK) relations to derive the real component, $\varepsilon_1$. Thereafter, the relative optical quantities such as the complex index of refraction can be calculated. Since a variety of optical processes are considered, the resultant complex DF will be valid for a wide spectral range from VIS to LWIR.

[1] A. Rogalski, J. Antoszewski, and L. Faraone, J. Appl. Phys. **105**, 091101 (2009).

[2] G. Ariyawansa, Y. Aytac, A. G. U. Perera, S. G. Matsik, M. Buchanan, Z. R. Wasilewski, and H. C. Liu, Appl. Phys. Lett. **97**, 231102 (2010).

[3] A. Majumdar, K. K. Choi, J. L. Reno, and D. C. Tsui, Appl. Phys. Lett. **86**, 261110 (2005).

[4] G. Ariyawansa, A. G. U. Perera, G. Huang, and P. Bhattacharya, Appl. Phys. Lett. **94**, 131109 (2009).

[5] H. C. Liu, M. Gao, J. McCaffrey, Z. R. Wasilewski, and S. Fafard, Appl. Phys. Lett. **78**, 79 (2001).

[6] R. C. Jayasinghe, G. Ariyawansa, N. Dietz, A. G. U. Perera, S. G. Matsik, H. B. Yu, I. T. Ferguson, A. Bezinger, S. R. Laframboise, M. Buchanan, and H. C. Liu, Opt. Lett. **33**, 2422 (2008).

[7] M. S. Ünlü and S. Strite, J. Appl. Phys. **78**, 607 (1995).

[8] A. L. Korotkov, A. G. U. Perera, W. Z. Shen, J. Herfort, K. H. Ploog, W. J. Schaff, and H. C. Liu, J. Appl. Phys. **89**, 3295 (2001).

[9] D. G. Esaev, M. B. M. Rinzan, S. G. Matsik, and A. G. U. Perera, J. Appl. Phys. **96**, 4588 (2004).

[10] Y. F. Lao, P. K. D. D. P. Pitigala, A. G. U. Perera, H. C. Liu, M. Buchanan, Z. R. Wasilewski, K. K. Choi, and P. Wijewarnasuriya, Appl. Phys. Lett. **97**, 091104 (2010).

[11] S. Murtaza, A. Srinivasan, Y. Shih, J. Campbell, and B. Streetman, Electron. Lett. **30**, 643 (1994).

[12] M.Born and E.Wolf, *Principles of Optics: Electromagnetic Theory of Propagation, Interference and Diffraction of Light*, 7th ed. (Cambridge University Press, Cambridge, England, 1999).

[13] Y.-F. Lao and A. G. U. Perera, J. Appl. Phys. **109**, 103528 (2011).

[14] B. F. Levine, J. Appl. Phys. **74**, R1 (1993).

[15] S. A. Stoklitsky, P. O. Holtz, B. Monemar, Q. X. Zhao, and T. Lundström, Appl. Phys. Lett. **65**, 1706 (1994).

[16] D. K. Sengupta, S. L. Jackson, D. Ahmari, H. C. Kuo, J. I. Malin, S. Thomas, M. Feng, G. E. Stillman, Y. C. Chang, L. Li, and H. C. Liu, Appl. Phys. Lett. **69**, 3209 (1996).

[17] H. C. Lin, K. L. Chang, K. C. Hsieh, K. Y. Cheng, and W. H. Wang, J. Appl. Phys. **92**, 4132 (2002).

[18] X. Hu, M. Li, Z. Ye, W. Y. Leung, K.-M. Ho, and S.-Y. Lin, Appl. Phys. Lett. **93**, 241108 (2008).

[19] M. S. Shishodia and A. G. U. Perera, J. Appl. Phys. **109**, 043108 (2011).

[20] Y.-F. Lao, C.-F. Cao, H.-Z. Wu, M. Cao, and Q. Gong, Electron. Lett. **45**, 105.

[21] C. M. Herzinger, B. Johs, W. A. McGahan, J. A. Woollam, and W. Paulson, J. Appl. Phys. **83**, 3323 (1998).

[22] T. Yamaguchi, H. Tamura, S. Taga, and S. Tsuchiya, Appl. Opt. **25**, 2703 (1986).